
APPLICABILITY OF METALENSES FOR GENERALIZABLE COMPUTER VISION

Yubo Zhang¹
yuboz4@uw.edu

Johannes Frösch¹
jfroech@uw.edu

Jinlin Xiang¹

Shane Colburn¹

Myunghoo Lee¹

Zhihao Zhou¹

Minho Choi²

Eli Shlizerman¹

Arka Majumdar¹
arka@uw.edu

¹University of Washington, Seattle, WA

²UNIST, South Korea

ABSTRACT

Optical neural networks (ONNs) are gaining increasing attention to accelerate machine learning tasks. In particular, static meta-optical encoders designed for task-specific pre-processing demonstrated orders of magnitude smaller energy consumption over purely digital counterpart, albeit at the cost of slight degradation in classification accuracy. However, a lack of generalizability poses serious challenges for wide deployment of static meta-optical front-ends. Here, we investigate the utility of a metalens for generalized computer vision. Specifically, we show that a metalens optimized for full-color imaging can achieve image classification accuracy comparable to high-end, sensor-limited optics and consistently outperforms a hyperboloid metalens across a wide range of sensor pixel sizes. We further design an end-to-end single aperture metasurface for ImageNet classification and find that the optimized metasurface tends to balance the modulation transfer function (MTF) for each wavelength. Together, these findings highlight that the preservation of spatial frequency-domain information is an essential interpretable factor underlying ONN performance. Our work provides both an interpretable understanding of task-driven optical optimization and practical guidance for designing high-performance ONNs and meta-optical encoders for generalizable computer vision.

Keywords Meta-Optics Encoder · End-to-end Optimization · Modulation Transfer Function(MTF)

1 Introduction

Diffraction optics leverage the high bandwidth of light and wavefront engineering to precisely modulate spatial light intensity, and have been widely applied to tasks such as imaging[1, 2, 3], beam shaping[4, 5, 6], filtering[7] and holography[8, 9]. With these physical capabilities, diffractive optical neural networks (ONNs)[10, 11, 12, 13] have been shown to offer advantages in massive parallelism, rapid inference[14], and energy efficiency[15, 16]. However, building a fully optical neural network remains highly challenging—not simply because of limited nonlinear operations[17] or programmability[18], but also because achieving advantages over modern electronic processors requires carefully leveraging multiple optical features simultaneously while avoiding a number of fundamental pitfalls[19]. A more feasible approach adopts a hybrid optical-electronic architecture, where a passive optical front-end preprocesses the input before feeding it into a digital back-end[20]. Such systems offload part of the computational burden to optics from the digital domain, achieving inference acceleration and energy savings at the cost of slight performance degradation compared to fully digital networks due to the information bottleneck imposed by the optical encoder.

Among various implementations of optical front-ends, meta-optics provides a compact and efficient solution[21]. Meta-optical encoders, built upon sub-wavelength-scale nano-structures, allow dense and parallel modulation of the amplitude, phase, and polarization of light, often achieving hundreds of optical operations on a single chip[22, 23, 24]. Under incoherent illumination, the image on sensor is the convolution of the incoherent object intensity and the point spread function (PSF) of the optical system[25, 26, 27]. Thus, by engineering the PSF of the meta-optics, we can implement different convolutions and effectively replace early convolutional layers in a neural network. Recent studies demonstrated that PSF-engineered meta-optical encoders, combined with advanced model compression techniques such as knowledge distillation[28, 29], can enable robust and energy-efficient ONNs for tasks such as classification[21] and segmentation[30, 31].

Although universal approximation theorem and neural tangent kernel (NTK) dynamics have theoretically shown that a sufficiently wide neural layer can approximate the behavior of deeper networks [32], in practice, most optical neural networks (ONNs) exhibit reduced task performance compared to their purely digital counterparts. Two major factors may contribute to this degradation. First, not all convolution kernels are physically realizable in optics. Even ignoring fabrication inaccuracies, the on-axis approximation introduces deviations between design and experiment [33]. Second, information loss during optical encoding irreversibly degrades the quality of input features, resulting in a lower performance even when followed by identical digital layers[15, 21, 30].

A promising strategy to mitigate the first limitation is end-to-end optimization[34, 35, 36, 37, 38, 39] (see Fig 1), where the meta-optical front-end and the digital back-end are jointly trained for task-specific application. This approach allows the system to adaptively compensate for optical constraints and imperfections, improving both the robustness and task performance of the hybrid architecture.

For the second limitation, although there are some information-theoretic tools[40, 41] to quantify representation efficiency, they often lack direct physical interpretation in optics. The modulation transfer function (MTF), in contrast, provides an intuitive and interpretable metric to analyze how spatial frequency content is preserved throughout an optical system.

In this work, we investigate the correlation between the task performance and MTF of the optical system, and show that for an incoherent imaging system, volume under MTF curve is highly correlated with the task performance. We compare the performance of the end-to-end optimized system with a benchmark using a fixed hyperboloid lens as the optical front end. The simulation results show that the optimized optical encoder not only achieves higher classification accuracy but also exhibits larger modulation transfer function (MTF) integrals than the hyperboloid design across a broad range of spatial frequencies within the cutoff frequency determined by the sensor pixel size. Moreover, we find the optimized metalens tends to balance the MTF over different wavelength channels, a trait we find useful for full-color imaging. To further test this correlation, we collect data using two optical front ends, an end-to-end designed lens originally optimized for full-color imaging and a hyperboloid meta-lens, and train identical digital backends on each dataset. The end-to-end optimized lens intended for imaging consistently outperforms the hyperboloid counterpart across a wide range of backend architectures and sensor pixel sizes. Moreover, we find that the task classification accuracy of the optimized metalens is similar to a high-end lens limited by the pixel resolution. This further supports our hypothesis that the MTF provides a good quantitative metric for ONN under incoherent illumination.

In summary, these results collectively demonstrate that the preservation of spatial frequency information plays a pivotal role in determining ONN performance. They highlight a fundamental link between frequency-domain preservation and task performance in ONNs, offering a unified perspective for analyzing and improving end-to-end optical-electronic co-designs.

2 Design Principle and Results

2.1 Design setup of end-to-end ONNs for experiments and simulations

We study a single-aperture, rotationally symmetric meta-optics that functions as an optical encoder, followed by a digital backend for ImageNet30 classification (a 30-class subset of ImageNet), as shown in Fig. 1a. As illustrated in Fig. 1b, the global design objective is either to maximize the final classification accuracy via end-to-end optimization or to optimize an MTF-based loss that incorporates imaging priors and physical constraints.

The former is conceptually straightforward since the ultimate goal of the hybrid system is to maximize classification accuracy. However, in practice, end-to-end optimization based on classification accuracy requires joint gradient descent over both the digital backend and the optical layer. This often causes the optical parameters to suffer from vanishing gradients due to the large depth of the digital network, preventing the phase variables from properly converging or leading them to get trapped in local minima (Supplementary 5.0.6).

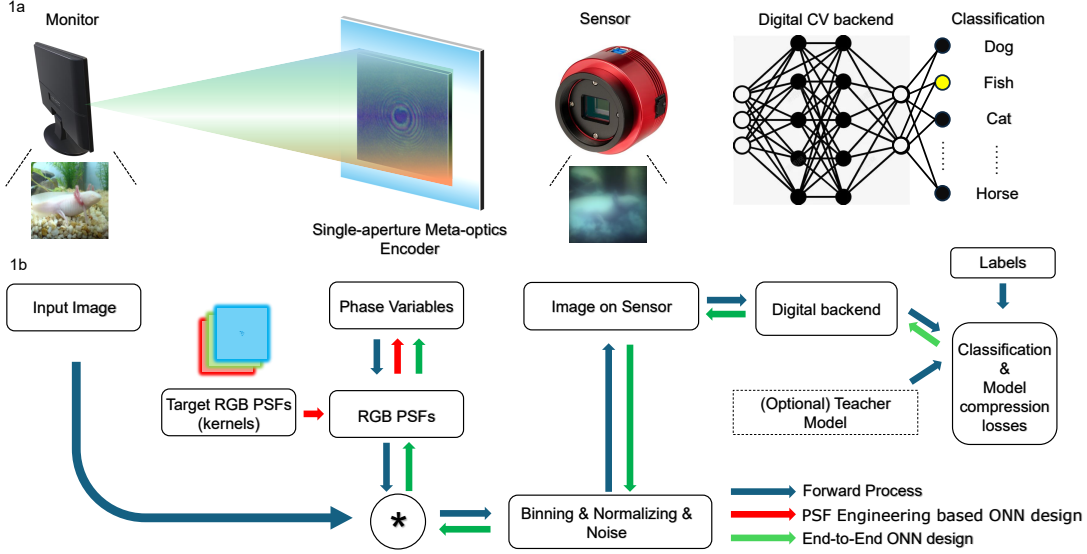


Figure 1: a. Schematic of the single aperture meta-optic encoder. An image of axolotl from ImageNet30 is displayed and encoded with the meta-optics, captured by a sensor and passed on to a downstream NN, where classification is performed. b. Schematic of end-to-end design and PSF engineering pipeline for a hybrid ONN system. The forward differentiable information propagation is indicated by blue arrows. The PSF-engineering-based ONN design follows the red arrows and involves two steps: first, retrieving the desired PSF(kernels). They may come from a convolution layer or some pure optical information priors; second, inversely designing the scatterer distribution on the meta-optics to match that particular PSF. In contrast, (green arrows) the end-to-end design jointly optimizes the optical encoder and the digital backend through a differentiable simulation pipeline, where sensor-plane signals are propagated to the digital network and the overall loss is minimized via gradient descent.

While the latter approach focuses on optimizing the optical encoder itself based on certain information prior. An example is maximizing the MTF integral product[42] to preserve spatial frequency content and achieve broadband imaging. However, the design approach does not account for how well the resulting optical output is perceived by the digital backend. This strategy generally leads to faster convergence and more stable optimization of the optical design, but the final classification accuracy ultimately depends on how well the digital network architecture aligns with the prior used for optical optimization.

Based on these 2 approaches, we conduct one experimental and one simulation study:

(1) Experimental setup. Experimentally, we use a 1-cm-aperture metalens designed for broadband imaging as the optical encoder, based on a design reported in [35]. A computer monitor displays incoherent image inputs, which are captured by a camera (ZWO ASI 678MC). The recorded optical outputs are then processed by a trainable digital neural network.

In the subsequent discussion, we refer to this device as the end-to-end lens, following the terminology of the original work, to distinguish it from our baseline hyperboloid lens. It should be noted that this lens is not optimized for classification; rather, its excellent broadband MTF characteristics align with the second case, where the design objective is guided by MTF-based imaging priors.

(2) Simulation setup. In simulation, we consider a 1-mm-aperture meta-optics as the optical encoder, jointly optimized with a digital backend in a fully end-to-end manner for image classification. All components of the system, including the optical propagation and sensor sampling, are modeled in a differentiable framework to enable gradient-based optimization. The smaller aperture is selected for computational efficiency, since larger apertures introduce more scattering elements and substantially increase the optimization cost.

Although experimental and simulated meta-optics don't directly match in size, they together highlight how the end-to-end optimization of the optical layer steers the MTF toward spatial frequency regions most relevant for classification.

This comparison provides physical insight into how task-oriented optical optimization links MTF shaping to downstream classification performance.

2.2 Hyperboloid Metalens Baseline: Motivation, Encoding Limitations, and Comparison with the End-to-End Design

For both setups, a hyperboloid lens operating at the green wavelength λ_0 is used as the baseline. The hyperboloid serves as a natural reference for evaluating the end-to-end optimized design, representing a conventional, analytically defined phase profile that focuses light according to geometric optics principles.

$$\phi(x, y) = \frac{2\pi}{\lambda_0} \left(f - \sqrt{x^2 + y^2 + f^2} \right)$$

With f denoting the focal length, the design formula of hyperboloid meta-optics simply maps the phase profile of the classic refractive lens' onto a plane. In the context of meta-optics, its imaging performance is fundamentally limited by phase-wrapping discontinuities in the phase profile.

The hyperboloid lens is not task-specific, as it is optimized solely for diffraction-limited imaging at λ_0 . By comparing it with the optimized meta-optics we can provide a quantitative metric to assess how much performance gain arises from the task-oriented end-to-end optimization or well-selected prior based MTF optimization.

To ensure a fair comparison, both hyperboloid and end-to-end lenses adopt rotational symmetry 5.0.5, implemented through a polynomial parameterization of the phase profile. This constraint, originally motivated by computational considerations, significantly accelerates optimization and enhances numerical stability. Beyond efficiency, rotational symmetry guarantees that any rotated field angle yields an identical, rotationally invariant PSF, simplifying the interpretation of optical behavior and enabling a clearer analysis of trends along the optical axis.

2.3 Characterization of 1-cm-aperture Metalens: MTF and Imaging Results

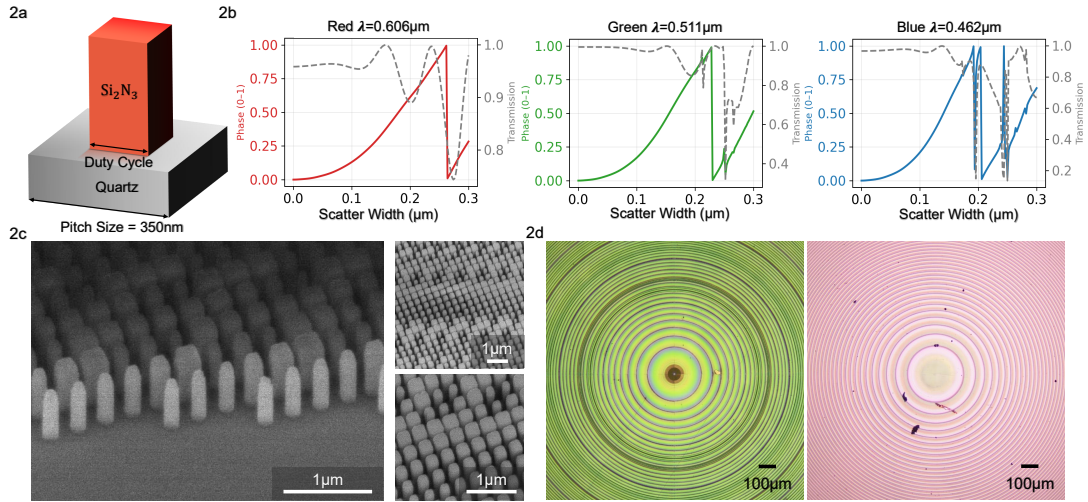


Figure 2: a. Schematic of a single scatterer in a 2D Si_3N_4 -on-quartz meta-optics array. b. RCWA simulation of the scatterer's phase and amplitude responses at red (606 nm), green (511 nm), and blue (462 nm) wavelengths. c. SEM images of the end-to-end designed meta-optics. d. Microscope images of the end-to-end designed meta-optics (left) and the hyperboloid benchmark (right).

The 1-cm-aperture meta-lenses (end-to-end and hyperboloid) were fabricated on a Si_3N_4 -on-quartz platform, as illustrated in Fig. 2a. Details of the fabrication process and experimental materials are provided in the supplementary

information (Section 5.0.1). The meta-atom responses are simulated using rigorous coupled wave analysis (RCWA) and are shown in Fig. 2b (scatterers designed at red (611 nm), green (532 nm), and blue (432 nm) wavelengths). A polynomial proxy function for the phase response is used for further design. Scanning electron micrographs and optical microscope images of the fabricated end-to-end and hyperboloid lenses are shown in Figs. 2c and 2d.

Figure 3a shows the RGB point spread functions of the two 1-cm-aperture meta-optics. The end-to-end imaging lens maintains consistently compact PSFs across red, green, and blue wavelengths, indicating balanced chromatic performance. In contrast, the hyperboloid lens tightly focuses only the green light, while the red and blue focal spots are noticeably defocused. The resulting spatially broadened PSFs severely degrade its color-imaging performance.

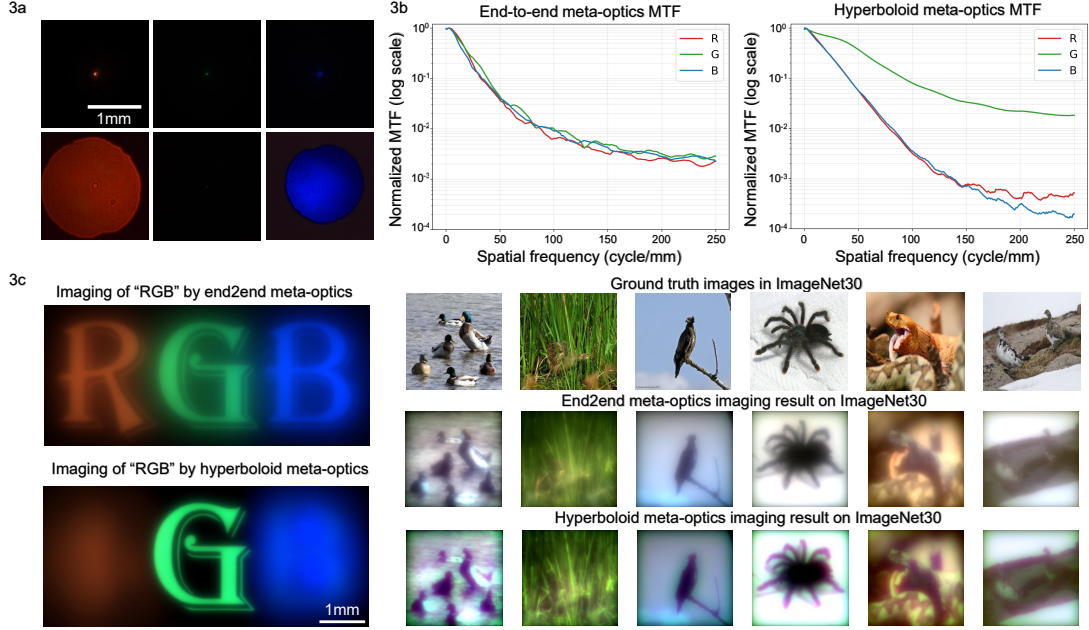


Figure 3: a. RGB PSFs of End-to-end lens (up) and hyperboloid lens (down). b. Log-scaled MTF of the end-to-end metalens(left) and hyperboloid metalens(right) c. (left) end-to-end(up)/Hyperboloid(down) metalens imaging results of an RGB pattern. (right) Captured images of ImageNet by end-to-end/hyperboloid metalens on sensor.

Figure 3b presents the experimentally measured modulation transfer function (MTF) curves, plotted on a logarithmic intensity scale. The MTF is obtained as the magnitude of the Fourier transform of the point spread function (PSF) and characterizes how well different spatial frequencies are captured by the optical system. When imaging under incoherent conditions, the MTF effectively serves as its frequency-domain filter. The horizontal axis, expressed in cycles per millimeter, corresponds to the actual spatial frequency up to the Nyquist limit determined by the detector pixel size (2 μm).

For the hyperboloid lens (right), only the green channel exhibits high MTF values across most spatial frequencies, while the red and blue channels suffer pronounced attenuation due to chromatic defocus. In contrast, the end-to-end design (left) demonstrates notably improved red and blue MTF curves, yielding a more spectrally balanced frequency response and a substantially higher average RGB MTF integral compared with the hyperboloid counterpart.

The two metalenses exhibit distinct imaging characteristics, as shown in Fig. 3c. The left panel shows single-wavelength imaging of RGB letter patterns, while the right panel presents broadband color imaging results. The hyperboloid lens produces sharper edges and higher local contrast due to well-corrected on-axis focusing at the design wavelength, but suffers from severe chromatic imbalance, with red and blue channels noticeably blurred. In contrast, the end-to-end optimized lens delivers more uniform color fidelity and balanced sharpness across channels—resulting in slightly softer edges yet a more consistent overall spectral response. This improvement enhances color fidelity and also leads to higher accuracy in downstream AI tasks (Fig. 4) as we show later.

2.4 Classification Accuracy of the 1-cm End-to-End Lens Across Different Sensor Pixel Sizes

In this section, we use the 1cm end-to-end lens for ImageNet30 classification and compare it against a hyperboloid lens across different digital back-ends (e.g. AlexNet and EffNet) and across multiple sensor pixel sizes (via binning).

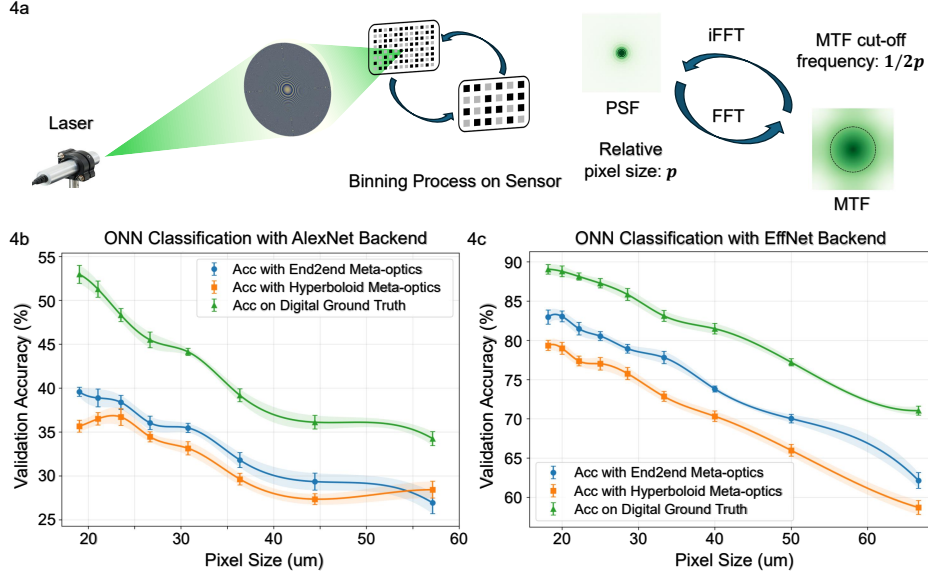


Figure 4: a. Increasing the sensor pixel size spatially averages the incident intensity, which reduces the resolvable PSF detail and consequently shifts the modulation transfer function (MTF) cutoff toward lower spatial frequencies. During end-to-end optimization with varying sensor pixel sizes, this sensor-imposed cutoff frequency defines the effective passband of the optical encoder, thereby determining which spectral regions of the MTF receive stronger optimization emphasis. b. Classification accuracy on ImageNet30 under different sensor binning levels, comparing (left) AlexNet and (right) EfficientNet digital back ends. Error bars denote accuracy variation across runs. Solid lines are visual aids for the trend and do not correspond to a theoretical prediction. Shaded regions visualize the accuracy spread and should not be interpreted as statistical confidence intervals.

Here, the 1cm end-to-end lens was optimized for broadband imaging by maximizing the MTF integral using a high-speed Rayleigh–Sommerfeld diffraction solver [35], yielding a wide spatial-frequency response with an extended effective passband across the visible spectrum.

In typical ONN designs, the detector pixel size directly influences the optimization process by setting the effective sampling resolution and determining the maximum spatial frequency that can be captured. As illustrated in Fig. 4a, larger pixels average the optical signal over a wider area, causing high variations of the optical field within each pixel to be lost and effectively reducing the MTF cutoff frequency. Consequently, as the pixel size increases, the system transmits a narrower spatial-frequency bandwidth, leading to degraded imaging fidelity.

Figures 4b and 4c show classification results using EfficientNet and AlexNet backends, representing strong and weak digital models widely used in the vision community. Each plot reports classification accuracy versus relative pixel size for the digital ground-truth, end-to-end metalens, and hyperboloid metalens. A consistent trend is observed: increasing the binning factor (i.e., using larger effective pixels) reduces accuracy for both systems due to the loss of high-frequency information. Conversely, higher sensor resolution enhances ONN performance by preserving finer spatial details, and in some cases, can even compensate for information loss in the optical layer.

Interestingly across different sensor binning sizes, the end-to-end optical encoder for broadband imaging consistently outperforms the hyperboloid design, demonstrating robustness to detector-resolution variations. The performance gap depends on the design of the digital backend: with the simpler AlexNet, the end-to-end advantage is smaller than that of

the more complex network, and both optical designs exhibit a larger degradation relative to the fully digital reference. In contrast, the higher-capacity EfficientNet better capitalizes on the richer frequency content preserved by the end-to-end optics, maintaining a clear advantage across all resolutions.

Since the optical layer contains far fewer trainable parameters compared with the subsequent digital backend, these results highlight the critical role of carefully designing the optical encoder in determining overall system performance. Moreover, because the end-to-end lens was optimized for broadband imaging, the findings further reinforce the strong correlation between the MTF of the optical front end and the achievable task accuracy. They also underscore the importance of frequency-domain information extraction and its tight coupling with the digital backend, showing that the optical encoder not only governs how information is transmitted but also affect how following digital network can utilize it.

2.5 Simulated End-to-End Metalens' MTF for Classification Objective

To complement the experimental study, we conducted numerical simulations of end-to-end meta-optics optimized under a different objective: the global target was set directly to maximize classification accuracy rather than broadband imaging, as in the 1-cm-aperture lens. For computational simplicity, the simulated lens employed a smaller 1 mm aperture and was jointly optimized with several digital neural-network backends. The sensor pixel size was also varied to investigate how the optimization adapts to different MTF cutoff frequencies.

The wavelength-dependent phase response (RCWA curves) was approximated using polynomial expansions (Supplementary Section 5.0.5), and light propagation was modeled in a differentiable manner to enable gradient-based optimization. During training, distinct learning rates and weight-decay coefficients were assigned to the phase variables and the digital-network parameters, as the magnitudes of the former are typically larger. This allowed us to monitor the evolution of the optical phase profile as the loss converged.

The meta-optic phase profile was initialized as a hyperboloid. After convergence, the end-to-end optimized model consistently achieved higher classification accuracy than its non-optimized counterpart (see Supplementary Fig. S5). Representative radial MTF curves and corresponding heatmaps are shown in Figs. 5a and 5b.

Compared with the initial hyperboloid phase, the end-to-end optimization exhibits two main trends. First, it balances the integrated MTF areas of the RGB channels—an expected outcome given that color images in typical datasets require uniform spectral performance for optimal classification. Second, the MTF converges toward the sensor's cutoff frequency, indicating that the network implicitly learns to allocate optical bandwidth within the detectable frequency range. This behavior suggests that the key mechanism behind classification-based end-to-end optimization for meta-optics encoder layer is the refinement of frequency-domain information represented by the MTF.

The resulting classification accuracies were consistent with those observed in the experimental 1-cm lenses, validating the relationship between the optical design objective, the modulation transfer characteristics, and the downstream task performance.

3 Discussion

The hyperboloid lens suffers from strong chromatic imbalance, whereas the end-to-end design slightly reduces sharpness but achieves better spectral balance. This balanced MTF improves color fidelity and correlates with higher downstream classification accuracy (Fig. 4). However, such advantages are not captured by conventional feature analysis—when images from both lenses are projected into a pretrained ResNet-50 feature space (Supplementary Section 5.0.4), they show similar separability, suggesting that standard deep features are insensitive to the subtle spectral and frequency-domain differences introduced by the optical front end.

Rather than pursuing state-of-the-art accuracy on a single downstream task, the goal of this work is to explore general principles of this performance gap, which essentially enables us for developing general design principles that extend beyond task-specific optimization.

To better capture these distinctions, we analyze the modulation transfer function (MTF) of each system to assess how frequency content is preserved. Rather than defining information content through feature separability in a pretrained network, the MTF characterizes information throughput as a frequency-domain filter. A key determinant of this throughput is the sensor pixel size, which sets the effective MTF cutoff frequency and constrains how much spatial-frequency content can be preserved by the optical encoder.

Our classification-based end-to-end simulations confirm the same MTF trends observed in the 1-cm broadband imaging lens, revealing that performance improvements stem from preserving a larger fraction of MTF energy within the

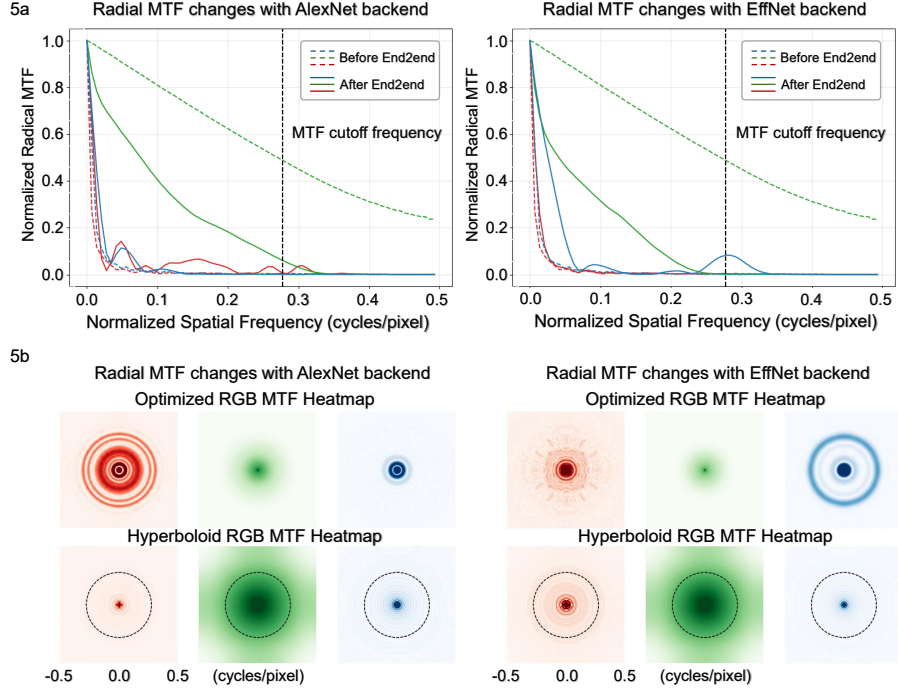


Figure 5: a. Radial MTF curves before (dashed RGB lines) and after (solid RGB lines) end-to-end optimization using AlexNet and EfficientNet backends. Both x-axes are expressed in relative spatial-frequency and normalized-MTF units. b. Corresponding logarithmic-scale heatmaps of the MTFs shown in a.

sensor’s cutoff frequency. This finding shows proof that the in-band MTF integral is a physically meaningful prior for quantifying the information retained by the optical encoder. Incorporating this prior make it possible to transform a complex end-to-end optimization problem into a more tractable MTF-based formulation, reducing the number of trainable parameters, improving convergence speed, and enhancing training stability by mitigating local minima.

4 Conclusion

In this work, we investigated a hybrid optical–electronic neural network comprising a single-aperture, rotationally symmetric meta-optics and a finite-pixel-size sensor, designed for a representative AI classification task. By systematically varying multiple hyperparameters, we identified a consistent optimization trend in end-to-end training: the optical front end tends to maximize the integrated modulation transfer function (MTF) within the sensor-imposed cutoff frequency.

Experimentally, we implemented a 1-cm-aperture metalens explicitly optimized for imaging through MTF maximization using a differentiable Rayleigh–Sommerfeld simulator. Compared with the hyperboloid baseline, the end-to-end lens exhibits more natural color rendition and a more balanced RGB MTF at the sensor plane. This balance allows the end-to-end encoder to preserve color information more faithfully and achieve higher classification accuracy across diverse digital back ends (e.g., AlexNet and EfficientNet). Notably, the performance gap remains robust under varying detector resolutions: even with increased pixel binning and corresponding loss of high-frequency content, the end-to-end encoder maintains a nearly constant advantage.

Together, these findings are consistent with our theoretical expectations and point toward a potential design principle for meta-optical encoders: emphasizing the in-band MTF integral under broadband operation may help preserve task-relevant spatial frequencies accessible to the digital backend.

While this study focused on a static, rotationally symmetric meta-optics for clarity and interpretability, the same end-to-end framework can naturally extend to richer optical parameterizations—such as multi-aperture arrays, field-dependent phase modulation, or polarization/coded spectral designs—and to joint sensor co-design including pixel geometry, color filter arrays, and binning strategies. Future work will explore task-adaptive fine-tuning built atop a general imaging-optimized encoder, as well as programmable or multiplexed meta-optics that sustain high MTF across

broadener spectral and angular bandwidths. These directions point toward scalable, physically interpretable pathways for integrating meta-optical front ends with modern machine perception systems.

Acknowledgments

References

- [1] Johannes E. Fröch, Luocheng Huang, Zhihao Zhou, Virat Tara, Zhuoran Fang, Shane Colburn, Alan Zhan, Minhó Choi, Arnab Manna, Andrew Tang, Zheyi Han, Karl F. Böhringer, and Arka Majumdar. Full color visible imaging with crystalline silicon meta-optics. *Light: Science & Applications*, 14(1), June 2025.
- [2] Xinjie Zhao, Xing Peng, Shaohui Xu, Shiqing Li, Hongbing Cao, and Feng Shi. Design of an infrared wide-angle metalens for medical endoscopic imaging systems. *Optics Express*, 33(14):29182–29196, 2025.
- [3] Yongcan Zeng, Xiaoling Ge, Yuqing Zhang, Siyang Xiao, Fen Zhao, Chongchong Ran, Mingjie Wu, Fengyuan Gan, Jiagui Wu, and Junbo Yang. Extended depth of focus metalens toward the entire long-wave infrared spectrum through inverse design framework. *Optics Express*, 33(18):39081–39091, 2025.
- [4] Shane Colburn and Arka Majumdar. Metasurface generation of paired accelerating and rotating optical beams for passive ranging and scene reconstruction. *ACS Photonics*, 7(6):1529–1536, May 2020.
- [5] Nanfang Yu and Federico Capasso. Flat optics with designer metasurfaces. *Nature materials*, 13(2):139–150, 2014.
- [6] Krishna Kumar, Borja Vidal, and Carlos Garcia-Meca. Metasurface based on phase change materials for electrically reconfigurable thz beam steering in copolarized transmission mode. *Scientific Reports*, 15(1):40666, 2025.
- [7] Joseph van der Gracht and Joseph N Mait. Incoherent pattern recognition with phase-only filters. *Optics letters*, 17(23):1703–1705, 1992.
- [8] Md Sadman Sakib Rahman and Aydogan Ozcan. Computer-free, all-optical reconstruction of holograms using diffractive networks. *ACS Photonics*, 8(11):3375–3384, October 2021.
- [9] Kaiyun Bi, Guanmao Zhang, Jilong Zhang, Guangchao Diao, Bochuan Xing, Mengjie Cui, Zhilin Ge, and Yuze Du. Reprogrammable metasurface holographic image encryption technology based on a three-dimensional discrete hyperchaotic system. *Optics Express*, 32(22):38703–38719, 2024.
- [10] Hanyu Zheng, Quan Liu, You Zhou, Ivan I Kravchenko, Yuankai Huo, and Jason Valentine. Meta-optic accelerators for object classifiers. *Sci. Adv.*, 8(30):eabo6410, July 2022.
- [11] Deniz Mengu, Yi Luo, Yair Rivenson, and Aydogan Ozcan. Analysis of diffractive optical neural networks and their integration with electronic neural networks. *IEEE Journal of Selected Topics in Quantum Electronics*, 26(1):1–14, 2020.
- [12] Jingtian Hu, Deniz Mengu, Dimitrios C Tzarouchis, Brian Edwards, Nader Engheta, and Aydogan Ozcan. Diffractive optical computing in free space. *Nature Communications*, 15(1):1525, 2024.
- [13] Sanaz Zarei. Programmable diffractive deep neural networks enabled by integrated rewritable metasurfaces. *Scientific Reports*, 15(1):35624, 2025.
- [14] Shiqi Chen, Yuhang Li, Yuntian Wang, Hanlong Chen, and Aydogan Ozcan. Optical generative models. *Nature*, 644(8078):903–911, 2025.
- [15] Luocheng Huang, Quentin AA Tanguy, Johannes E Fröch, Saswata Mukherjee, Karl F Böhringer, and Arka Majumdar. Photonic advantage of optical encoders. *Nanophotonics*, 13(7):1191–1196, 2024.
- [16] Tingzhao Fu, Jianfa Zhang, Run Sun, Yuyao Huang, Wei Xu, Sigang Yang, Zhihong Zhu, and Hongwei Chen. Optical neural networks: progress and challenges. *Light: Science & Applications*, 13(1):263, 2024.
- [17] Ying Zuo, Bohan Li, Yujun Zhao, Yue Jiang, You-Chiuan Chen, Peng Chen, Gyu-Boong Jo, Junwei Liu, and Shengwang Du. All-optical neural network with nonlinear activation functions. *Optica*, 6(9):1132–1137, 2019.
- [18] Loubnan Abou-Hamdan, Emil Marinov, Peter Wiecha, Philipp del Hougne, Tianyu Wang, and Patrice Genevet. Programmable metasurfaces for future photonic artificial intelligence. *Nature Reviews Physics*, pages 1–17, 2025.
- [19] Peter L. McMahon. The physics of optical computing. *Nature Reviews Physics*, 5(12):717–734, October 2023.
- [20] Minhó Choi and Arka Majumdar. Free-space optical encoder for computer vision. *npj Nanophotonics*, 2(1):36, 2025.

- [21] Minho Choi, Jinlin Xiang, Anna Wirth-Singh, Seung-Hwan Baek, Eli Shlizerman, and Arka Majumdar. Transferable polychromatic optical encoder for neural networks. *Nat. Commun.*, 16(1):5623, July 2025.
- [22] Mark L Brongersma, Ragip A Pala, Hatice Altug, Federico Capasso, Wei Ting Chen, Arka Majumdar, and Harry A Atwater. The second optical metasurface revolution: moving from science to technology. *Nature Reviews Electrical Engineering*, 2(2):125–143, 2025.
- [23] Shun Wen, Xinyuan Xue, Shuai Wang, Yibo Ni, Liqun Sun, and Yuanmu Yang. Metasurface array for single-shot spectroscopic ellipsometry. *Light: Science & Applications*, 13(1):88, 2024.
- [24] Aun Zaidi, Noah A Rubin, Maryna L Meretska, Lisa W Li, Ahmed H Dorrah, Joon-Suh Park, and Federico Capasso. Metasurface-enabled single-shot and complete mueller matrix imaging. *Nature Photonics*, 18(7):704–712, 2024.
- [25] Kaixuan Wei, Xiao Li, Johannes Froech, Praneeth Chakravarthula, James Whitehead, Ethan Tseng, Arka Majumdar, and Felix Heide. Spatially varying nanophotonic neural networks. *Science Advances*, 10(45):eadp0391, 2024.
- [26] Joseph W Goodman, AR Dias, and LM Woody. Fully parallel, high-speed incoherent optical method for performing discrete fourier transforms. *Optics Letters*, 2(1):1–3, 1978.
- [27] Md Sadman Sakib Rahman, Xilin Yang, Jingxi Li, Bijie Bai, and Aydogan Ozcan. Universal linear intensity transformations using spatially incoherent diffractive processors. *Light: Science & Applications*, 12(1):195, 2023.
- [28] Jinlin Xiang, Shane Colburn, Arka Majumdar, and Eli Shlizerman. Knowledge distillation circumvents nonlinearity for optical convolutional neural networks. *Applied Optics*, 61(9):2173–2183, 2022.
- [29] Yuetian Jia, Chao Qian, Zhixiang Fan, Tong Cai, Er-Ping Li, and Hongsheng Chen. A knowledge-inherited learning for intelligent metasurface design and assembly. *Light: Science & Applications*, 12(1):82, 2023.
- [30] Jinlin Xiang, Minho Choi, Yubo Zhang, Zhihao Zhou, Arka Majumdar, and Eli Shlizerman. Neural tangent knowledge distillation for optical convolutional networks. *arXiv preprint arXiv:2508.08421*, 2025.
- [31] Sandra Virbukaitė, Jolita Bernatavičienė, and Daiva Imbrasienė. Glaucoma identification using convolutional neural networks ensemble for optic disc and cup segmentation. *IEEE Access*, 12:82720–82729, 2024.
- [32] Jinlin Xiang and Eli Shlizerman. Tkil: tangent kernel approach for class balanced incremental learning. *arXiv preprint arXiv:2206.08492*, 2022.
- [33] Joel Yeo, N Duane Loh, Ramon Paniagua-Dominguez, and Arseniy I Kuznetsov. Eigencwd: a spatially varying deconvolution algorithm for single metalens imaging. *Optics Express*, 33(13):28481–28492, 2025.
- [34] Ethan Tseng, Shane Colburn, James Whitehead, Luocheng Huang, Seung-Hwan Baek, Arka Majumdar, and Felix Heide. Neural nano-optics for high-quality thin lens imaging. *Nature communications*, 12(1):6493, 2021.
- [35] Johannes E Fröch, Praneeth Chakravarthula, Jipeng Sun, Ethan Tseng, Shane Colburn, Alan Zhan, Forrest Miller, Anna Wirth-Singh, Quentin AA Tanguy, Zheyi Han, et al. Beating spectral bandwidth limits for large aperture broadband nano-optics. *Nature communications*, 16(1):3025, 2025.
- [36] Gaurav Arya, William F Li, Charles Roques-Carmes, Marin Soljacic, Steven G Johnson, and Zin Lin. End-to-end optimization of metasurfaces for imaging with compressed sensing. *ACS Photonics*, 11(5):2077–2087, 2024.
- [37] Carlos Mauricio Villegas Burgos, Tianqi Yang, Yuhao Zhu, and A Nickolas Vamivakas. Design framework for metasurface optics-based convolutional neural networks. *Applied Optics*, 60(15):4356–4365, 2021.
- [38] Julie Chang, Vincent Sitzmann, Xiong Dun, Wolfgang Heidrich, and Gordon Wetzstein. Hybrid optical-electronic convolutional neural networks with optimized diffractive optics for image classification. *Scientific reports*, 8(1):12324, 2018.
- [39] Yunhui Zeng, Haopeng Zhong, Zhenwei Long, Hongkun Cao, and Xin Jin. From performance to structure: a comprehensive survey of advanced metasurface design for next-generation imaging. *npj Nanophotonics*, 2(1):39, 2025.
- [40] Leyla A Kabuli, Henry Pinkard, Eric Markley, Clara S Hung, and Laura Waller. Designing lensless imaging systems to maximize information capture. *arXiv preprint arXiv:2506.08513*, 2025.
- [41] Henry Pinkard, Leyla Kabuli, Eric Markley, Tiffany Chien, Jiantao Jiao, and Laura Waller. Information-driven design of imaging systems. *arXiv preprint arXiv:2405.20559*, 2024.
- [42] Luocheng Huang, Shane Colburn, Alan Zhan, and Arka Majumdar. Full-color metaoptical imaging in visible light. *Advanced Photonics Research*, 3(5):2100265, 2022.

5 Supplement

5.0.1 Material and Fabrication

The metaslenses (Fig. S1) were fabricated on a Si_3N_4 -on-quartz platform using standard nanofabrication techniques. First, a thin Si_3N_4 film was deposited onto a quartz substrate to serve as the high-index layer. A positive electron-beam resist was then spin-coated, followed by electron-beam lithography to define the square scatterer array pattern across the full 1 cm aperture. After development, the resist served as an etch mask for reactive ion etching (RIE), transferring the designed nanostructure geometry into the Si_3N_4 layer with high fidelity. Residual resist was removed by solvent cleaning and oxygen plasma ashing. The resulting metasurface exhibited uniform structural quality over the centimeter-scale area, confirmed by optical microscopy (radially equal structural color) and scanning electron microscopy from both top-view and oblique angles. This straightforward geometry (Si_3N_4 square pillars on quartz) is inherently compatible with scalable nanoimprint lithography, making the process well suited for mass manufacturing in foundry environments.



Figure S1: Images of our end-to-end lens(right) and hyperboloid(left) lens used for experiment. Their apertures are designed to be identically 1cm

5.0.2 Experimental Setup

Figure S2 illustrates the experimental setup used to measure the point spread functions (PSFs) of the two lenses. Single-wavelength laser sources (red, green, and blue) from Thorlabs are used individually as illumination. After passing through a 25 μm pinhole, the beams become approximately collimated, as the distance between the aperture and the meta-optics is sufficiently large. The PSFs are then captured at the image plane using a ZWO ASI 678 MC camera.

During the ImageNet30 data acquisition process, a DELL monitor was placed at the original pupil position to display the target images. Using an automated capture pipeline, we collected approximately 36 000 encoded images for both the hyperboloid and end-to-end lenses, without applying any color rebalancing. The exposure time was dynamically adjusted to prevent saturation.

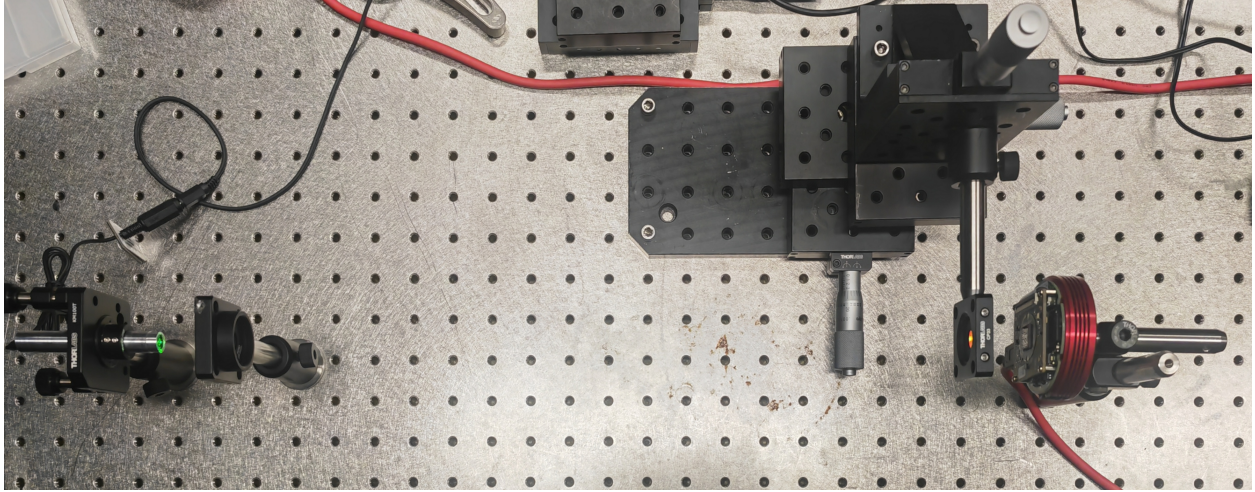


Figure S2: Our experimental setup schematic of PSF measuring and data capturing.

5.0.3 Imaging results of End-to-end designed lens and hyperboloid lens

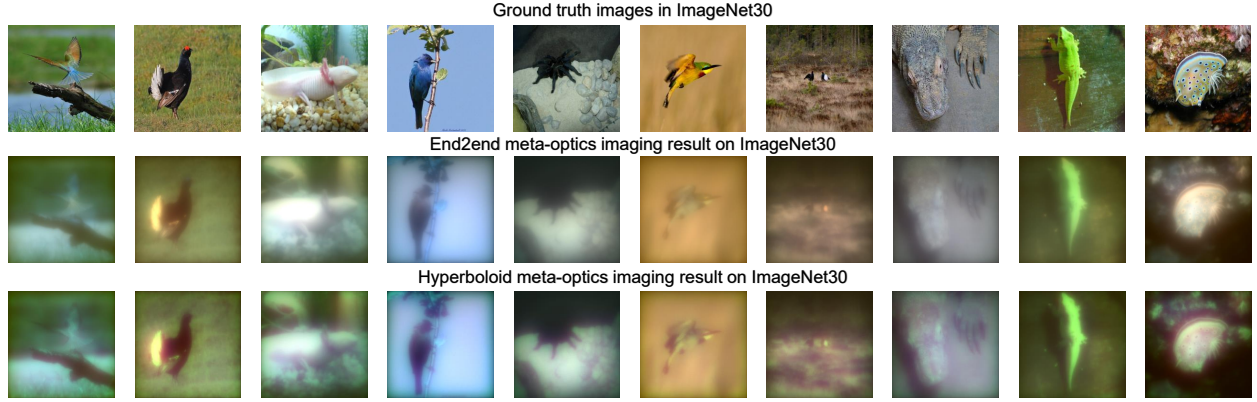


Figure S3: Imaging comparison of an end-to-end metalens and the hyperboloid lens with same aperture and f -number. Top: Digital ground truth. Middle: End2end lens’ imaging results showing superior color fidelity and smooth tonal rendering. Bottom: hyperboloid result with sharper contours but reduced color fidelity due to broadband chromatic effects.

We compare the end-to-end designed metalens with a baseline hyperboloid metalens of the same aperture and f -number. Supplementary Fig. S3 shows (top) the digital ground-truth reference, (middle) the end-to-end lens imaging outputs, and (bottom) the hyperboloid lens imaging results. Qualitatively, the end-to-end lens preserves higher color fidelity and smoother global intensity gradients across the field, with reduced inter-channel crosstalk and more accurate saturation in chromatic regions. In contrast, the hyperboloid lens yields crisper contours and stronger high-frequency edge contrast, but at the expense of color accuracy—exhibiting desaturation and mild hue shifts consistent with residual broadband chromatic aberrations and channel-dependent MTF roll-off. Overall, the end-to-end design provides more faithful color reproduction, whereas the hyperboloid lens emphasizes geometric detail (edges/contours). These qualitative trends are consistent across the dataset and align with our system characterization.

5.0.4 Clustering results of optically encoded sensor images

To assess how different meta-optics encoders preserve the dataset’s information, we visualize feature distributions at the sensor plane. We pass the experimentally captured images from the end-to-end lens and the hyperboloid lens as well as the digital ground truth through a frozen ImageNet-pretrained ResNet-50 encoder, followed by k -means clustering while sweeping the number of clusters K . We report Normalized Mutual Information (NMI) as a function of K . The two optical encoders yield broadly similar curves (Fig.S4), with the hyperboloid lens slightly higher at large K . This suggests that, when features are extracted by a generic (mismatched) backbone, the class-separable structure recoverable from sensor-plane measurements is comparable across the two front ends, with a minor advantage to the hyperboloid likely reflecting conventional imaging statistics that better align with convolutional inductive biases. Given that their final evaluation accuracy has large difference, this indicates that a ResNet-based feature extractor does not reliably capture the amount of information preserved by the optical encoder, even though the hyperboloid lens may produce sharper edges in conventional imaging terms. These observations motivate our shift toward physically grounded, frequency-domain characterization via the modulation transfer function (MTF).

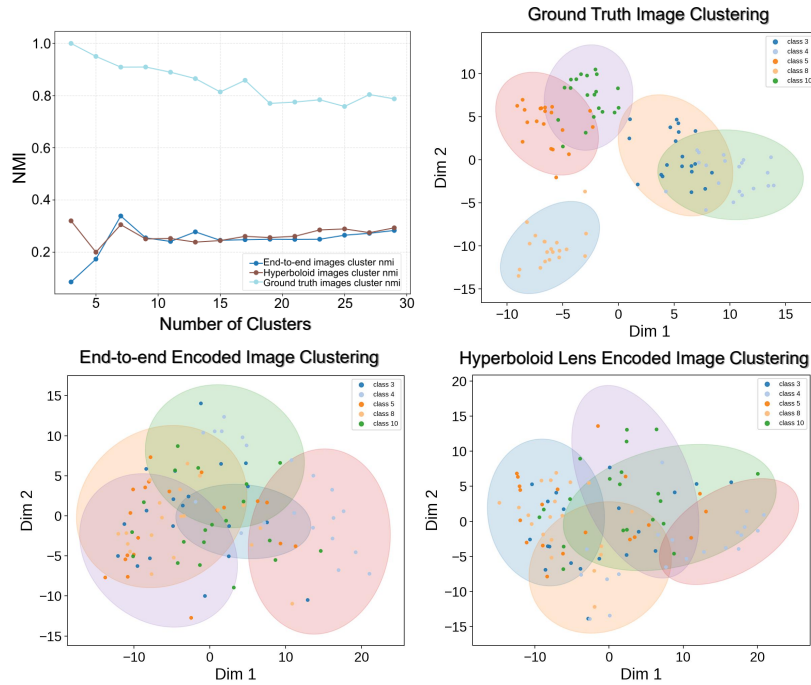


Figure S4: (Upper left) Normalized Mutual Information (NMI) versus number of clusters K for the end-to-end optimized optical encoder and the hyperboloid lens. Both yield similar trends. (Other panels) Clustering results under three conditions: (Upper Right) Clustering of digital ground truths (ARI=1.000, Normalized Mutual Information(NMI)=1.000). (Lower left) Clustering after passing through the end-to-end encoder (ARI=0.102, NMI=0.214). (Lower right) Clustering after the hyperboloid encoder(ARI=0.154, NMI=0.282). All results are obtained at the sensor plane, reflecting the information-preserving ability of different encoders before the digital backend.

5.0.5 Methods of the end-to-end optimization

This section details the training-time optical-digital co-design. We model three wavelengths (R, G, B). The trainable optical variables are the rotationally symmetric phase coefficients for green, parameterized as

$$\phi_G(r) = \sum_{k=0,2,4,6\dots}^K c_k r^k, \quad r \in [0, 1],$$

where r is the normalized pupil radius and $\mathbf{c} = \{c_k\}$ are optimized. To couple the three channels through fabrication constraints, we precompute wavelength-dependent responses via RCWA and use them as differentiable surrogates. Specifically, we fit a smooth inverse map $s(r) \approx \mathcal{F}_G^{-1}(\phi_G(r))$ from green phase to scatter geometry (e.g., meta-atom size/shape) using a low-order polynomial, and then obtain red/blue phases by forward maps $\phi_\lambda(r) \approx \mathcal{F}_\lambda(s(r))$ for $\lambda \in \{R, B\}$. These surrogate mappings are implemented with differentiable polynomial expansions to enable backpropagation.

Given $\{\phi_\lambda\}$, we compute the wavelength-wise PSFs $h_\lambda(d; \mathbf{c})$ with a scalar diffraction solver (e.g., Fresnel/AS). For a scene at distance d , we render the sensor-plane image by a distance-dependent, approximately shift-invariant blur:

$$y_\lambda = x_\lambda * \mathcal{S}_d(h_\lambda(d; \mathbf{c})), \quad y = \sum_{\lambda \in \{R, G, B\}} \gamma_\lambda y_\lambda + \eta,$$

where \mathcal{S}_d scales the kernel according to imaging geometry, γ_λ models spectral weighting (illumination/QE), and η denotes sensor noise. The convolutional approximation holds in the isoplanatic regime; when the object is extremely far, the effective image extent can become small relative to the PSF support (yielding a degenerate, PSF-like pattern), and when the object is very close, off-axis aberrations and field dependence break shift-invariance, in which case a spatially varying convolution would be more accurate. In practice we train within distances where the approximation is acceptable.

The rendered RGB image y is fed to a digital backbone $f_\theta(\cdot)$ to produce the task output (e.g., class logits). We minimize a task loss (e.g., cross-entropy) jointly over optical coefficients and network weights,

$$\min_{\mathbf{c}, \theta} \frac{1}{N} \sum_{i=1}^N \mathcal{L}(f_\theta(y_i(\mathbf{c})), t_i) + \lambda_{\text{reg}} \mathcal{R}(\mathbf{c}),$$

with optional regularizers \mathcal{R} (e.g., phase smoothness or bandwidth constraints). All steps—phase parametrization, RCWA-based surrogates, PSF generation, rendering, and the digital network—are differentiable, enabling standard gradient-based optimization.

In training, we assign *distinct learning rates* to the optical phase variables and the digital backbone: the phase coefficients \mathbf{c} are updated with step size η_c and the network weights θ with η_θ (typically $\eta_c < \eta_\theta$), implemented via optimizer parameter groups (e.g., Adam):

$$\mathbf{c} \leftarrow \mathbf{c} - \eta_c \nabla_{\mathbf{c}} \mathcal{L}, \quad \theta \leftarrow \theta - \eta_\theta \nabla_{\theta} \mathcal{L}.$$

5.0.6 MTF interpretability of end-to-end optimization

We analyze how end-to-end optimization reshapes the spatial-frequency response of the metalens relative to a conventional hyperboloid baseline. Consistent with Fig. S5, panel (a) shows that the end-to-end (E2E) optimized encoder provides higher classification accuracy across a range of sensor binning levels in simulation, motivating a closer inspection of two representative settings— 70×70 and 190×190 . Panels (b–d) evaluate the corresponding optical properties. For each binning configuration, we visualize the optimized MTF heatmaps and compare radial MTF slices against those of the initial hyperboloid lens, annotating the MTF cutoff frequency set by the virtual pixel size, which is controlled by the chosen binning factor.

In both the 70×70 and 190×190 cases, the end-to-end design produces a more balanced and uniform in-band MTF across the RGB channels, whereas the hyperboloid exhibits stronger inter-channel variation and less consistent frequency support.

Panels (e–f) show the evolution of the learned phase coefficients over 200 training epochs, by which point both the loss and evaluation accuracy have already converged. Interestingly, the phase variables continue to exhibit substantial fluctuations even after the objective has stabilized. This behavior suggests that end-to-end optical optimization may settle into local minima or plateau regions of the loss landscape where multiple optical configurations yield similar downstream task performance.

Overall above simulated results on the 1-mm-aperture metalens highlight a key fragility of end-to-end optimization: many phase configurations produce nearly identical task performance, causing the optimization to settle in local minima or flat regions of the loss landscape. This instability underscores that the in-band MTF—rather than the specific optimized phase profile—is the more reliable and physically interpretable indicator of information preserved by the optical encoder.

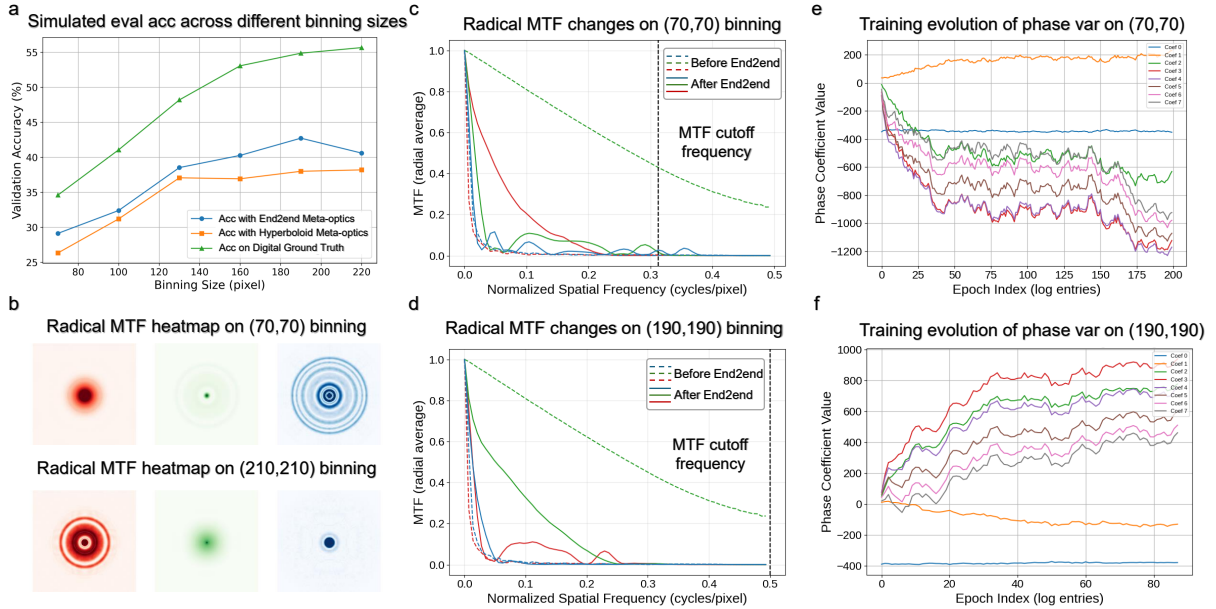


Figure S5: (a) Accuracy improvement of the end-to-end optimized encoder over the hyperboloid lens across different binning sizes. We further examine two representative settings— 70×70 and 190×190 —to analyze their post-optimization optical properties. (b) Heatmaps of the optimized MTF profiles for the 70×70 and 190×190 binning configurations. (c–d) Comparison of the optimized MTF slices (solid) against the initial hyperboloid MTF (dashed) for 70×70 (top) and 190×190 (bottom). (e–f) Evolution of the learned phase coefficients during training for the 70×70 (top) and 190×190 (bottom) cases. Both models were trained for 200 epochs to ensure convergence of loss and evaluation accuracy.

5.0.7 More classification accuracy results

We perform end-to-end simulations (with hyperboloid as initial phase profile) on the ImageNet30 classification task across different digital back-end architectures and evaluate their corresponding MTF integral improvement and accuracy improvement. Due to the relatively small aperture size used in our simulations, the overall improvement margin over the hyperboloid baseline is modest. Nevertheless, all instances exhibit higher accuracy when the green channel's MTF integral is rebalanced relative to the red and blue channels. We also observe that stronger backend models (e.g., ResNet) are able to extract more information in the frequency domain, leading to larger end2end validation-accuracy gains compared with weaker models (e.g., AlexNet). These results still highlight our conclusion and meanwhile suggest that the choice of digital back-end architecture is an essential factor influencing ONN performance, motivating further exploration of optimal backend designs.

	Alexnet	Effnetb0	Effnetb7	Resnet18	Resnet50	vgg11	vgg19
Digital accuracy(%)	37.80	77.60	77.60	67.53	70.47	69.40	69.33
Hyperboloid simulated accuracy(%)	28.27	64.60	65.93	52.93	56.87	54.33	52.73
End-to-end simulated accuracy(%)	29.87	66.73	67.13	56.40	60.53	55.27	57.00
Red MTF integral improvement(%)	618.89	56.61	75.31	305.02	34.03	1208.26	184.97
Green MTF integral improvement(%)	-65.41	-59.09	-84.09	-43.53	-46.60	-85.46	-89.61
Blue MTF integral improvement(%)	105.75	136.49	292.00	46.76	120.22	260.45	181.18

Table 1: Comparison of accuracy and MTF metrics across different Digital backends.